Published in final edited form as:
Nanomedicine (Lond). 2014 June ; 9(8): 1209–1222. doi:10.2217/nnm.13.84.

Targeting of Pancreatic Cancer with Magneto-Fluorescent Theranostic Gold Nanoshells

Wenxue Chen[1,2,†], **Ciceron Ayala-Orozco**[3,†], **Nrusingh C. Biswal**[1], **Carlos Perez-Torres**[4], **Marc Bartels**[1], **Rizia Bardhan**[3], **Gary Stinnet**[4], **Xian-De Liu**[5], **Baoan Ji**[6], **Amit Deorukhkar**[7], **Lisa V. Brown**[3], **Sushovan Guha**[8], **Robia G. Pautler**[4], **Sunil Krishnan**[7], **Naomi J Halas**[3,9], and **Amit Joshi**[1,a]

[1]Division of Molecular Imaging, Department of Radiology, Baylor College of Medicine, Mail: BCM 360, One Baylor Plaza, Houston, TX 77030 (USA)

[2]Department of Diagnostic Imaging, The Fourth Hospital of Hebei Medical University/Hebei Province Tumor Hospital, 12 Jiankang Road, Shijiazhuang, Hebei Province 050011 (China)

[3]Department of Chemistry, Rice University, 6100 Main St, Houston, TX 77005

[4]Department of Molecular Physiology and Biophysics, Baylor College of Medicine, One Baylor Plaza, Houston, TX 77030

[5]Department of Genitourinary Medical Oncology, The University of Texas MD Anderson Cancer Center, 1515 Holcombe Blvd., Houston, TX 77030

[6]Department of Biochemistry and Molecular Biology, Guggenheim 13-21B. Mayo Clinic, 200 First Street S.W., Rochester, MN 55905

[7]Department of Radiation Oncology, Division of Radiation Oncology, The University of Texas MD Anderson Cancer Center, 1515 Holcombe Blvd., Houston, TX 77030

[8]Department of Gastroenterology, Hepatology and Nutrition, The University of Texas MD Anderson Cancer Center, 1515 Holcombe Blvd., Houston, TX 77030

[9]Department of Electrical and Computer Engineering, Rice University, 6100 Main St, Houston, TX 77005

Abstract

Aim—We report a magneto-fluorescent theranostic nanocomplex targeted to neutrophil gelatinase associated lipocalin (NGAL) for imaging and therapy of pancreatic cancer.

Materials and Methods—Gold nanoshells resonant at 810 nm were encapsulated in silica epilayers doped with iron oxide and the NIR dye ICG, resulting in theranostic gold nanoshells (TGNS), which were subsequently conjugated with antibodies targeting NGAL in AsPC-1-derived xenografts in nude mice.

[a]Reprint requests: Amit Joshi, Ph.D., Baylor College of Medicine, MS 360, One Baylor Plaza, Houston, TX 77030, amitj@bcm.edu, Phone: (713)7989191.
[†]Equal contributing first authors

Disclosure of Potential Conflicts of Interest
No potential conflicts of interest were disclosed.

Results—AntiNGAL-conjugated TGNS specifically targeted pancreatic cancer cells *in vitro* and *in vivo* providing contrast for both NIR fluorescence and T2 weighted MR imaging with higher tumor contrast than can be obtained using long-circulating but non-targeted PEGylated nanoparticles. The nanocomplexes also enabled highly specific cancer cell death via NIR photothermal therapy *in vitro*.

Conclusions—Theranostic gold nanoshells with embedded NIR and MR contrasts can be specifically targeted to pancreatic cancer cells with expression of early disease marker NGAL, and enable molecularly targeted imaging and photothermal therapy.

Keywords

nanoshells; optical imaging; photothermal; pancreatic cancer; noninvasive imaging; MRI

Introduction

Pancreatic cancer is the fourth leading cause of cancer-induced mortality in the United States, accounting for 36,800 estimated fatalities in 2010 [1]. Its dismal five-year survival rate of 5% is attributed primarily to rapid metastasis and to a lack of reliable tumor markers for early diagnosis. Among patients without metastatic disease, less than 20% are surgically resectable, the only potentially curative treatment, which still confers only a 15–25% rate of 5-year overall survival [2]. Other patients are frequently treated with chemo-radiation therapy with 5-year overall survival rates of 5–10% [3, 4]. Current therapies, alone or in combination, have done little to improve the grim outlook, since pancreatic cancer has low response to chemotherapy, and develops resistance to gemcitabine, the standard first-line chemotherapeutic agent for advanced stage disease [5]. The development of a method for detection and therapy of early stage pancreatic cancer, immune to drug resistance, would be immensely helpful for improving the chance of survival.

Cancer nanotechnology developments in the area of theranostic probes (combined diagnosis and therapy) provide an attractive avenue for detecting and treating pancreatic cancer [6–10]. Recently we demonstrated the theranostic capabilities of multifunctional magneto-fluorescent silica core-gold nanoshells for diagnosis and photothermal therapy of cancer [11–13]. These agents are comprised of a silica core with a thin gold layer whose thickness can be varied to tune the plasmon resonance wavelength of the nanoparticle into the NIR wavelength region, where light penetration in tissue is maximal. In addition to photothermal therapy, these complexes enhance the fluorescence of the only FDA cleared NIR dye Indocyanine Green (ICG) by up to 50X, resulting in a biocompatible, yet stable and bright NIR fluorescence with imaging performance comparable to the semiconductor quantum dots. As the outcome of pancreatic cancer surgery strongly depends on the margin status, deployment of magneto-fluorescent theranostic probes for image guided surgery/thermal therapy can favorably impact the care of pancreatic cancer patients.

For maximal impact on pancreatic cancer, the emerging cancer theranostics should be targeted to early stage malignancies. However, there is a scarcity of early stage tumor biomarkers for pancreatic cancer along with the lack of clinical validation [14–18]. Recently, neutrophil gelatinase-associated lipocalin (NGAL) has been detected in pancreatic

cancer tissue and it has been clinically investigated as a marker for early diagnosis of pancreatic intraepithelial neaoplasia [19, 20]. NGAL has been reported to be up-regulated up to 27 times in pancreatic cancer cells [19]. NGAL expression is also up-regulated in multiple human cancers including breast, colorectal, ovarian, thyroid carcinomas, prostate and bladder [21–27], implying that NGAL may have a critical role in solid tumor formation. In particular, strong NGAL over-expression has been observed in early stage pancreatic cancer lesions, suggesting that it is a marker for early dysplasia in pancreas and an attractive target for cancer theranostic nanoprobes.

We report that silica-gold-iron-oxide magneto-fluorescent TGNS complexes can be used for combined image contrast and photothermal therapy of pancreatic cancer overexpressing NGAL. The agent was comprised of a silica core-gold shell nanoshell with an additional silica epi-layer encapsulating approved NIR (ICG) and MR (iron oxide) contrast agents. The agents were targeted to NGAL-overexpressing cells via antibodies conjugated to the external surface of the complex. Nanocomplex dimensions were tuned to provide a plasmon resonance at ~808 nm, coinciding with the emission maximum of the fluorescent dye ICG, and thus enhancing its quantum yield by ~50X. The resulting probe acted as an NIR imaging agent when illuminated with 785 nm light, and as a photothermal therapy agent when illuminated with 808 nm light. We identified the efficacy of TGNS for image contrast and therapy of pancreatic cancer *in vitro* and *in vivo* on disease models created with AsPC-1, a human pancreatic adenocarcinoma cell line known to overexpress NGAL. *In vitro* MRI and fluorescence optical imaging (FOI) verified the enhanced specific binding of NGAL targeted TGNS to AsPC-1 cells. We also report the lack of cytotoxicity of these constructions and nearly 100% efficiency in ablation of the cancer cells upon exposure to NIR radiation at 808 nm. *In vivo* MRI and FOI imaging studies on nude mice with AsPC-1 xenografts were conducted to demonstrate the favorable biodistribution of NGAL targeted TGNS to tumors following systemic delivery.

Materials and Methods

In vitro Fluorescence Optical Imaging

The purpose of in vitro imaging was to validate the targeting efficacy and specificity of antiNGAL-TGNS for NGAL expressing pancreatic cancer cells by standard immunohistochemistry techniques. AsPC-1 (human, pancreas, adenocarcinoma, derived from metastatic ascites) cells were grown in RPMI 1640 medium with 2.05 mM L-Glutamine (HyClone), 1% Antibiotic-Antimycotic and 10% FBS. Cells were incubated at 37°C in a 5% CO_2 environment and detached from culture with 0.05% trypsin /0.53mM EDTA, then resuspended in media for passaging to wells. 3×10^5 cells of ASPC-1 were plated in each well of 4 well plates respectively, and allowed to incubate. Subsequently, cells were washed with 1×PBS twice and fixed with PFA (3.7% paraformaldehyde in PBS). Cells were then permeabilized with 0.2 % triton, following which they were washed twice with PBS. 10% NGS solution was added to each well plate and incubated for 15 min. The cells were divided into three groups: The NGAL group (AsPC-1 incubated with antiNGAL-conjugated TGNS with concentration 2×10^9 particles/mL 2 h at 4°C) was the experimental group while the blocked group (AsPC-1 incubated with antiNGAL-conjugated TGNS after

blocking NGAL with antiNGAL, 20 μg/mL, 1 h at 4°C then washed three times with PBS 5min) and the unconjugated TGNS group (AsPC-1 cells incubated with unconjugated TGNS for 2 h at 4°C) were the controls. After 2 h, the cells were washed with PBS to remove unbound nanocomplexes, after which the secondary antibody, Goat Anti-Rabbit IgG-Alexa Fluor 488 (Invitrogen) was added to the wells and incubated for 1 h at 4°C. The cells were again washed with PBS while protected from light for excess secondary antibody removal. The cell plates were then mounted on slides with mounting media containing DAPI (Invitrogen) and prepared for fluorescence imaging. To acquire the fluorescence images, we used a Leica fluorescence microscope (DM6000 B; Leica Microsystems GmbH) with a 100 W xenon lamp and specific filters. The images were obtained using cutoff filters with appropriate excitation/emission wavelengths (laser excitation/emission wavelengths 360/470 nm (DAPI), 480/530 nm (Alexa Fluor 488), and 720/820 nm (ICG).

In vitro MR Imaging

1×10^6 AsPC-1 cells were plated in each well of 60×15 mm style cell culture dishes and allowed to incubate with the TGNS as described in the previous section. After 2 h of incubation with the nanocomplexes, the cells were washed with PBS, followed by scraping the cells from the bottom of the petri dish, dispersed in 500 μL PBS, and centrifuged at 1100 rpm for 5 min. The supernatant was then removed, leaving ~100 μL cells containing antiNGAL-conjugated TGNS and unconjugated TGNS in the Eppendorf tubes, respectively. 500 μL of 0.5% agarose gel was added to each tube and the samples were left at 4°C for 10 min to allow the agarose to solidify. The tubes with the nanocomplexes suspended within the gel containing the solidified agarose gel with AsPC-1 cells were directly utilized for MR Imaging. MRI experiments were performed on a Bruker Avance Biospec, 9.4 T spectrometer, 21 cm bore horizontal imaging system (Bruker Biospin, Billerica, MA) with a 35 mm volume resonator. *In vitro* imaging of cells suspended in agarose was performed using a 3D RARE (rapid acquisition with relaxation enhancement) sequence with a repetition time (TR) of 2000 ms, an echo time (TE) of 20 ms (TR/TE equal to 2000/20 ms) with a RARE factor of 8 leading to an effective TE of 60 ms. FOV was 25.6×25.6×12.8 mm with an acquisition matrix of 128×128×64 yielding an isotropic 200 μm resolution. Maximum intensity projections were created from the 3D MRI data using a threshold segmentation approach in MATLAB® (2008a, The Mathworks, Natick, MA). The threshold was set at the average minus twice the standard deviation of the sample. Pixels under this value were considered to be hypointense and labeled as black in the image. The surrounding normotense agarose was labeled as a transparent light green. Each hypointense pixel contains a cluster of labeled cells, since the scan resolution was not sufficient to identify individual cells.

In vitro Photothermal Therapy and Cytotoxicity Studies

AsPC-1 cells were grown in a 4 well plate and divided into three groups, as described earlier. 5×10^5 cells were incubated at 37 °C with nanocomplexes (2×10^9 particles/mL) for 2 h and then washed with PBS. Photothermal ablation was performed using an NIR laser diode at 808 nm (L808P200, Thorlabs Inc.) for 10 min at a power density of 5.81 W/cm^2 and a spot size of ~0.8mm diameter. After irradiation, cells were rinsed gently with PBS and incubated at 37 °C with media for 4 h. Cell viability was assessed using Calcein to stain live

cells and propidium iodide (PI) to stain dead cells. For cytotoxicity studies, cells were incubated at 37 °C with antiNGAL-conjugated TGNS, free antiNGAL followed by antiNGAL-conjugated TGNS, and unconjugated TGNS, these cells were not illuminated with the NIR laser. After incubating the cells with Calcein/PI mixture for 30 min at 37°C, a cover slip was mounted and the cells were imaged. The images were obtained using excitation/emission wavelengths 480/530 nm (Calcein), 520/620 nm (PI).

The AsPC-1 xenograft model—The protocol for xenograft tumor creation and nude mice imaging was approved by the Institutional Animal Care and Use Committee (IACUC) of Baylor College of Medicine.

Athymic Nude-Foxn1nu female mice (4–6wk of age, 20±3g, Harlan) were injected s.c. on the right flank with 4×10^6 cells per mouse, AsPC-1 cells suspended in 0.2ml serum-free medium. After 14 days, tumors grew to about 8–12mm in diameter. Intravenous administration of nanocomplexes in mice was conducted in two stages. In the first stage, the specificity of antiNGAL-TGNS for the AsPC-1 xenografted tumors was determined. Mice were randomized into an experimental group (n=7) and a control group (n=6). Mice treated with antiNGAL-conjugated TGNS comprised the experimental group. As a control, mice were treated with free antiNGAL antibody (250 μg in 200 μL of saline injected through the tail vein) to block NGAL 4 hours prior to injecting antiNGAL-conjugated TGNS. In both cases, nanocomplexes were administered *via* 200 μL tail vein injections with concentration of 5×10^9 particles/mL. In a second set of experiments the time dependent NIR/MR imaging was compared between antiNGAL-conjugated TGNS and PEGylated TGNS to evaluate the contrast advantages of targeting over passive accumulation in tumor by enhanced permeability and retention (EPR) affect due to PEGylation. Mice were randomized into an antiNGAL-TGNS treated group (n=6) and PEGylated-TGNS treated group (n=6).

Fluorescence Imaging Method

Mice were placed in a clear plastic chamber and isoflurane delivered in concentrations of 1–3% in oxygen (up to 5% for initial induction). To maintain body heat of the mice during anesthesia, we utilized a heating pad and temperature controller (FHC Bowdoin, ME, USA). Whole body fluorescence images at 0.5 h, 2 h, 4 h, 24 h, 48 h, and 72 h post-injection were acquired using a homebuilt NIR imaging system consisting of an image-intensified cooled CCD camera (Princeton Instruments) outfitted with a 28 mm Nikkor (Nikon) lens. Image acquisition was controlled by customised MATLAB routines (The MathWorks, Inc.) from an off-the-shelf personal computer (Dell Optiplex 760). Excitation light was generated with a 100 mW near infrared (NIR) laser diode at 785 nm (Thorlabs, Inc.) and diffused with a planoconvex lens and a light shaping diffuser (both Thorlabs, Inc.). For capturing excitation light images we used a neutral density filter with optical density (OD) 3 (Andover Corporation). A fluorescence band pass filter at (830 ± 20) nm (Andover Corporation) in combination with a holographic notch filter (OD 6) at 785 nm (Kaiser Optical Systems, Inc.) was employed for collecting fluorescence emission light while rejecting excitation leakage, as suggested by Hwang et. al [28]. From the images, regions of interests (ROIs) were manually selected around the tumor and non-tumor sites. The ratios of the fluorescence intensities from these ROIs were then calculated.

In vivo MRI Methodology

Animals were anesthetized with gaseous isoflurane at 1–3% in oxygen, then placed into a mouse holder within the magnet. During imaging, the animal body temperature was maintained at 37°C, continually monitored with a rectal probe using an animal warmed-air heating system (SA Instruments, Stony Brook, NY). Imaging was performed with a multislice RARE (rapid acquisition with relaxation enhancement) sequence with a TR/TE equal to 2805/20 ms with a RARE factor of 6 leading to an effective TE of 60 ms. The imaging sequence included a 5 ms fat suppression pulse. FOV was 30×30 mm with 20 slices at 1 mm thickness. The acquisition matrix of 256×256 yielded an in-plane isotropic 117 μm resolution. The transverse relaxation time T2 weighting sufficient for detection of superparamagnetic iron oxide. Qualitative criteria for the diagnosis of tumor were based on the identification of single or multiple focal zones of increased or decreased signal tumor intensity. Signal tumor intensity measurements were scaled to image noise, and tumor intensity compared before and after injection of nanocomplexes.

Results

TGNS characterization

The TGNS complexes were chemically synthesized by a stepwise multi-layered deposition process as described in supplementary information. The correct assembly and functionality of each layer was characterized. A schematic illustration of the assembly process of antibody (anti-NGAL) conjugation to TGNS is depicted in Fig. 1A. The binding of Iron Oxide to gold nanoshells and localization inside silica layer was confirmed by TEM (supplementary information Fig. S1). Fluorescence emission from the ICG doped inside the silica is provided in Fig. S2B. The size of the TGNS is ~180 nm according to TEM measurements (Fig. 1B). FTIR spectra of the streptavidin-conjugated TGNS and controls (bare-TGNS and streptavidin) were obtained to confirm the binding of streptavidin to the bare-TGNS (Fig. 1C). The peak at 3303 cm^{-1} corresponds to the N-H stretching mode present in streptavidin and in the conjugated TGNS but absent in bare-TGNS. In addition, the peaks at 1521 cm^{-1} (N-H bending mode) and 1635 cm^{-1} (C=O stretching mode) increase in intensity after streptavidin conjugation to the bare-TGNS. Quantification of the number of antibodies on anti-NGAL conjugated TGNS by ELISA is significantly higher than that of the control (bare-TGNS), as shown in Fig. 1D. These nanocomplex characteristics support the expected conjugation of antiNGAL-biotin to TGNS using the streptavidin-biotin interaction. Further characterization of TGNS bioconjugation is provided in supplementary information (Fig. S2) including optical properties, zeta potential and hydrodynamic diameter.

AntiNGAL-conjugated TGNS bind pancreatic cancer cells *in vitro* to facilitate photothermal therapy

The efficacy of antiNGAL TGNS for binding to NGAL expressed in pancreatic cancer cells was studied via FOI and T2-weighted MR imaging of cultured AsPC-1 cells. Fluorescence microscopy results are illustrated in Fig. 2A. The antiNGAL-conjugated TGNS preferentially bound to cells over-expressing NGAL vs the blocked group, and the unconjugated-TGNS treated group. 2-D MR images showed that the number of hypointense

pixels of AsPC-1 cells labeled with antiNGAL-conjugated TGNS (Fig. 2B) was higher than that observed with the blocked group and with the unconjugated-TGNS. The accompanying thresholded 3-D MR images gave a visual representation of the distribution of nanocomplex-conjugated cells. The brown spots represent the nanocomplex-labeled cells and the surrounding green regions represent the agarose medium. As the imaging studies were performed on fixed cells, these experiments only validated the specific binding of antiNGAL TGNS to immobilized NGAL expressed on AsPC-1 cells. *In vitro* NIR photothermal therapy/cytotoxicity experiments were conducted with live cells and results showed that almost complete cell death in the laser treated region was observed for AsPC-1 cells labeled with antiNGAL-conjugated TGNS (Fig. 2C). Such an effect was not observed for the blocked group, nor for the unconjugated TGNS treated group, which further validated the specific binding of antiNGAL TGNS, this time in live cells. In the cytotoxictiy studies, the NIR laser was not applied and cell death was not significantly observed in the experimental group, and neither in the two control groups. This verifies that the gold nanoshell based cancer therapy observed was of an externally controlled nature (induced by incident NIR laser light).

AntiNGAL-conjugated TGNS enhances accumulation in tumor possibly by interacting with NGAL

To study the specificity of antiNGAL-conjugated TGNS targeting of pancreatic tumors and the impact of molecular targeting on biodistribution of ~180 nm nanocomplexes, we used NIR-FOI for tracking the fluorescence contrast evolution in the two groups of mice with NGAL overexpressing xenografts. The results are illustrated in Fig.3, for a representative animal from each group. Group 1 was comprised of mice treated with antiNGAL-conjugated TGNS (Fig. 3A, bottom row), and the control group comprised of mice treated with NGAL-blocked by prior free antiNGAL injection (Fig. 3A, top row). Mice were imaged at 0.5 h, 2 h, 4 h, 24 h, 48 h and 72 h post-injection. The images are depicted in a pseudocolor scale with intensities normalized with respect to the maximal value for the experimental group mice, which demonstrated the maximum fluorescence in tumors among the two groups. Substantial differences in fluorescence contrast variation within the mice bodies, especially between the targeted and NGAL blocked cases are clear. Qualitatively, the fluorescence intensity in the tumor was lower for the blocked mice. To account for variations across animals and imaging conditions, Tumor-to-Background Ratio (TBR) were computed by selected tumor and normal ROIs from each image. TBR was plotted vs time for the two groups in Fig. 3B. The TBR variation is significant between the two groups ($p=0.0177$), while the variation across time points is not significant ($p=0.0779$), which is expected, since the TBR is more or less constant from 24 to 72 hours. The results suggest that targeting NGAL overexpression increases the NIR fluorescence contrast in tumors by 60–70% at 24 hours after injection and is indicative of enhanced accumulation in tumors for NGAL targeted particles.

While NIR images are strongly surface weighted due to multiple scattering and attenuation related losses from deep tissue signal, the iron oxide component of the nanocomplexes enables the observation of 3D spatial variations via T2-weighted MR imaging. Each of the mice was imaged in a small animal MR scanner after NIR imaging. Iron oxide is a negative

contrast agent, where the image intensity is lowered in areas of nanocomplex accumulation. A representative image of the tumor central cross section for the mice from the NGAL blocked group, and the experiment group at 24 hours post-injection is depicted in Fig. 4A and 4B, respectively. A water phantom was placed along with the mice to allow normalization to account for unintentional variations in scanning conditions. The experimental group image demonstrates greater lowering of T2 intensity of the tumor relative to the water control (T2 Intensity reduced to 41.41% of water control intensity) compared to the NGAL blocked group (T2 Intensity reduced to 82.52% of water control intensity). For quantitative comparison of nanocomplex biodistribution and to account for statistical variation across animals and imaging conditions, the tumor ROIs were manually segmented from each reconstructed slice, and the tumor-to-body T2 intensity was determined, which was then averaged over all slices. The obtained tumor-to-body ratio was averaged over mice in each group and plotted in Fig. 4C. It is clear that the accumulation of nanocomplexes in tumors is increased by targeting NGAL, and the overall trend is similar to that obtained in NIR fluorescence images, with the difference that in MR the cross-sections of the tumors have been analyzed and there is no surface weighing as in NIR imaging. The relative contrast between T2 intensity ratios is approximately 30% at 24 hours post-injection, compared to 60–70% in case of NIR, which is expected as NIR imaging is more sensitive.

To analyze the biodistribution of nanocomplexes in different organs and infer information about their bio-elimination, the animals were sacrificed at 72 hours post-injection and the resected organs were imaged with the NIR imaging system under conditions identical to *in vivo* imaging, as illustrated in Fig.5 (A, B). The highest fluorescence intensities were observed in tumors of the experimental group compared to the NGAL blocked control group. The luminous intensity on the unit surface area of each tissue suggested that the tumors have a higher nanocomplex uptake compared to other tissue. To quantitatively determine the biodistribution, the Au content in each organ was measured by ICP-MS (Fig. 5C). The results corresponded well to the fluorescence intensities reported in Fig. 5B, with the exception of liver and spleen, which have high NIR absorption and as a result the fluorescence from the accumulated nanocomplexes is internally absorbed and not registered with the imaging system. The ICP-MS results demonstrated the specificity of antiNGAL conjugated nanocomplexes for targeting NGAL overexpressing pancreatic cancer cells *in vivo*. As expected, tissues of the overexpressing NGAL xenografts have higher nanocomplex accumulation than the blocked group. Consistently with this observation strong light scattering in dark-field microscopy corresponding to gold nanoshells were localized in tumor tissue with the targeted TGNS, compared to the blocked NGAL controls (Fig. 5D). Immunohistochemical staining of tumor sections verified the strong NGAL expression, and vascularized nature of xenografted AsPC-1 tumors. (supplementary information Fig. S3) Mean tumor accumulation of nanocomplexes for antiNGAL-TGNS injected mice was twice as high compared to animals with prior injections of free antibody. The statistical variation across experimental groups ($p=0.0045$) was significant for ICP-MS quantification of the gold level in tumors. The measured Au levels in lungs and heart may be due to the residual blood left behind in these highly perfused tissues. Both fluorescence and ICP-MS

measurements show low Au concentration in brain, indicating that the nanocomplexes have low permeation through the blood-brain-barrier, probably due to their size.

Performance of antiNGAL-conjugated TGNS versus PEG-TGNS on imaging

The second set of in vivo experiments investigated the performance of long circulating PEG-TGNS agents vs antiNGAL-TGNS agents, which were also PEGylated following antiNGAL conjugation. Passive accumulation of nanoparticles in tumors using PEG-TGNS was compared against the active NGAL targeting effect of the antiNGAL-TGNS (Fig. 6). The TBR with the antiGNAL-TGNS is significantly higher than the PEG-TGNS across all imaging time points (Fig. 6A, 6B), suggesting there is an effect on active NGAL targeting using anti-NGAL. In addition, the antiNGAL-conjugated TGNS result in a greater lowering of T2 intensity on the pancreatic tumor compared to the only the PEG conjugated TGNS (Fig. 6C, 6D). The temporal behavior of T2 contrast in Fig. 6D is different from Fig 4C for time points after 24 hrs. While strong contrast differences between PEG-TGNS and antiNGAL-TGNS are clear at early timepoints, compared to Fig. 4C, the tumors from experiment group lost contrast after 24 hours. This may be because of fluctuations in MR measurements arising from differences in positioning of mice from day to day, the possibly lower iron-oxide loading of nanoparticles in this batch resulting in reduced sensitivity, or lower uptake in this batch of tumors.

Discussion

The nanocomplex presented here integrates targeting, diagnosis, and photothermal therapy all within the same nanostructure. The complimentary features of high sensitivity NIR molecular imaging and high resolution 3D MR imaging are both enhanced by integration into the theranostic nanostructure. The immunotargeting allowed the antiNGAL-conjugated TGNS to specifically attach to pancreatic cancer cells over-expressing NGAL in amounts up to four times more than in the case of blocked NGAL, or unconjugated TGNS, under *in vitro* settings. Moreover, photothermal therapy *in vitro* was shown to effectively ablate the cancer cells only when the nanocompex was antiNGAL-conjugated. Both unconjugated and antiNGAL-conjugated nanocomplexes were not toxic to the cells in the absence of 808 nm NIR illumination, confirming the externally modulated nature of nanocomplex-mediated photothermal therapy. Recently the toxicity of gold nanoshells has been evaluated extensively including cytotoxicity, pyrogenecity, genotoxicity, hemolysis, systemic toxicity and intracutaneous reactivity without any indication of toxicity in any of the studies [29].

Similar trends for NGAL targeting were observed *in vivo* by NIR-FOI and MRI. Imaging experiments validated the specific binding of antiNGAL-TGNS to tumors as a consistent higher contrast both in NIR and MR imaging was observed for mice injected with antiNGAL-TGNS compared to when mice were pre-injected with free antiNGAL. Both techniques complemented each other, as FOI showed higher sensitivity than MRI. However, MRI allowed imaging of tumor cross-sections with high 3D spatial resolution. The nanoparticle biodistribution studied by FOI in each organ and ICP-MS also confirmed quantitatively that nanoparticle uptake within the tumor is enhanced by NGAL targeting. ICP-MS also revealed that the nanoparticles accumulate in liver and spleen in substantial

amounts which was anticipated since particles > 10 nm are scavenged by the macrophages of the reticuloendothelial system and accumulate in liver and spleen [30, 31]. The enhancement in imaging contrast was again observed when antiNGAL-TGNS were compared with PEG-TGNS. It should be noted that antiNGAL-TGNS were also PEGylated, However, PEG-TGNS agents in spite of having a longer circulation time, showed inferior contrast in tumors especially at the early time points, possibly because of their extended circulation half life. The tumor to body ratio was seen to exceed unity for PEG-TGNS (Fig. 6D) and antiNGAL-TGNS (Fig. 4C) when prior injections of free antibody was performed. This indicated higher amounts of TGNS in circulation compared to accumulation in tumors.

Even as our targeting strategy against NGAL on the pancreatic cancer cell line AsPC-1 was effective in the mouse xenograft model, numerous challenges remain for clinical translation. NGAL is typically stored in neutrophil granules, and is present systemically, which can adversely impact bio-distribution in humans. The rationale for using NGAL for targeting pancreatic cancer is three fold: (i) There is a scarcity of biomarkers for early stage pancreatic cancer, when the disease has the best response to treatment, (ii) NGAL is significantly (27 fold) overexpressed in pancreatic cancer, compared to normal pancreatic tissue and acute pancreatitis, and (iii) nanocomplexes targeting NGAL are inherently non-cytotoxic and can be locally activated only by application of NIR light, with NIR/MR imaging guidance.

Many other biological events have been discovered to be associated with NGAL, such as inhibition of bacterial iron uptake, renal injury, and mediation of inflammatory activity [32–35]. Moreover, NGAL is associated with human atherosclerotic lesions by forming a NGAL-MMP-9 complex which prolongs matrix metalloproteinase-9 activity [36–38] and thus recently NGAL targeting with nanoparticles has been demonstrated for MRI studies of the atherosclerotic plaque [39]. Since, we employed antihuman NGAL targeted TGNS in a mouse model, the contrast in xenografted human tumors was maximized, however, in the artherosclerotic plaque imaging study reported in reference [38], antimouse NGAL antibody (vs antihuman NGAL in the present study) was employed for targeting magnetic micelles to vascular disease sites in a genetically engineered mouse, and irrespective of systemically distributed mouse NGAL, MR image contrast in plaque with NGAL overexpression was achieved. The fact that NGAL is up-regulated in certain injury and inflammatory states can potentially reduce the effectiveness of proposed agents and lead to off-target effects, and the discrimination of cancer can be difficult in chronic pancreatitis patients. However, it has been reported that in the context of Pancreatic Cancer, NGAL levels progressively increase with disease progression, but decrease in advanced stages of the disease (stage-4) [19]. Hence the proposed probe will be suited for early stage interventions, when chemo-radiation therapy induced injury to internal organs is not present.

In summary, antiNGAL-conjugated TGNS are promising candidates for diagnosis and treatment of pancreatic cancer, especially in early stages when NGAL over-expression is significant. Fully exploited, the proposed theranostic nanocomplexes can contribute to lowering the morbidity and mortality associated with pancreatic cancer.

Future Perspectives

The results presented in this study pave the way towards photothermal therapy in an *in vivo* tumor graft under FOI/MRI guidance. In this imaging focused study, the injected TGNS concentration was limited to ~5e9 particles/ml, which is more than two orders of magnitude lower than concentration used in prior studies on gold nanoparticle mediated photothermal therapy [9] hence prospects of successful image guided photothermal therapy are bright. However, a major challenge for targeting pancreatic cancer with nanoparticles irrespective of the targeting mechanism is circumventing the intense stroma, and desmoplastic reactions around the pancreatic cancer lesions [40], which are not replicated in the subcutaneous xenograft tumor model. The current NGAL targeted TGNS embodiments at >150nm diameter, while successful in generating high NIR and MR contrast, may not have optimal penetration in orthotopic tumors. Overcoming tumor transport barriers is a multifaceted undertaking with nanoparticle size expected to have a significant role. Current research efforts are underway to reproduce NIR plasmon resonance, NIR fluorescence enhancement, and MR contrast in 50–100nm particle sizes, by utilizing alternate geometries including nanosphere inside a nanoshell (nanomatryoshka), or hollow gold nanoshells [41, 42]. A key technology for multimodal contrast enabled photothermal therapeutic agents is the deposition of reproducible and tunable width silica layers on gold surfaces, which was demonstrated in this paper for silica core gold nanoshells, but can be adapted for gold nanoparticles in other size regimes.

Supplementary Material

Refer to Web version on PubMed Central for supplementary material.

Acknowledgments

We give thanks to Alex Urban for help with dark-field microscopy, J.T. Mayo and Emily Day for their assistance with ICP-MS. We give thanks to Sabrina Herrera, and Sufeng Mao for their assistance with IHC & HE staining.

Grant Support

We gratefully acknowledge the funding support provided by the NIH grants U01 CA151886, and R01CA151962 to Amit Joshi, Wenxue Chen, Nrusingh Biswal and Marc Bartels. Ciceron Ayala, Rizia Bardhan and Naomi J. Halas were supported by the DoD NSSEFF, the Air Force Office of Scientific Research (F49620-03-C-0068) and Robert A. Welch Foundation (C-1220 and C1222) and U01 CA151886. Carlos Perez-Torres and Robia Pautler were supported by NIH grant P30DK079638.

Abbreviations

NGAL	Neutrophil gelatinase-associated lipocalin
GNS	Gold nanoshells
TGNS	Theranostic gold nanoshells
ICP-MS	Inductively Coupled Plasma-Mass Spectrometry
ICG	Indocyanine Green
MR	Magnetic Resonance

MRI	Magnetic resonance imaging
MMP	Matrix metalloproteinase
FOI	Fluorescence optical imaging
ICP	Inductively coupled plasma
TEOS	Tetraethyl orthosilicate
PEG	Polyethylene glycol
MPTES	Mercaptopropyl triethoxysilane
ELISA	Enzyme-linked immunosorbent assay
HRP-AR	Anti-rabbit IgG-linked horseradish peroxidase
TMB	Tetramethylbenzidine
PFA	Paraformaldehyde
IACUC	Institutional Animal Care and Use Committee
NIR	Near infrared
OD	Optical density
ROIs	Regions of interests
TBR	Tumor-to-Background Ratio

References

Papers of special note have been highlighted as:

* of interest

1. Jemal A, Siegel R, Ward E, et al. Cancer statistics, 2008. CA Cancer J. Clin. 2008; 58(2):71–96. [PubMed: 18287387]
2. Sener SF, Fremgen A, Menck HR, Winchester DP. Pancreatic cancer: A report of treatment and survival trends for 100,313 patients diagnosed from 1985–1995, using the national cancer database. J. Am. Coll. Surg. 1999; 189(1):1–7. [PubMed: 10401733]
3. Krishnan S, Rana V, Janjan NA, et al. Prognostic factors in patients with unresectable locally advanced pancreatic adenocarcinoma treated with chemoradiation. Cancer. 2006; 107(11):2589–2596. [PubMed: 17083124]
4. Krishnan S, Rana V, Janjan NA, et al. Induction chemotherapy selects patients with locally advanced, unresectable pancreatic cancer for optimal benefit from consolidative chemoradiation therapy. Cancer. 2007; 110(1):47–55. [PubMed: 17538975]
5. Bafna S, Kaur S, Momi N, Batra SK. Pancreatic cancer cells resistance to gemcitabine: The role of muc4 mucin. Brit. J. Cancer. 2009; 101(7):1155–1161. [PubMed: 19738614]
6. Yang L, Mao H, Cao Z, et al. Molecular imaging of pancreatic cancer in an animal model using targeted multifunctional nanoparticles. Gastroenterology. 2009; 136(5):1514–1525. e1512. [PubMed: 19208341]
7. Chen Y, Bathula SR, Li J, Huang L. Multifunctional nanoparticles delivering small interfering RNA and doxorubicin overcome drug resistance in cancer. J. Biol. Chem. 2010; 285(29):22639–22650. [PubMed: 20460382]

8. Gultepe E, Reynoso FJ, Jhaveri A, et al. Monitoring of magnetic targeting to tumor vasculature through MRI and biodistribution. Nanomedicine-UK. 2010; 5(8):1173–1182.
9. Dreaden EC, MacKey MA, Huang X, Kang B, El-Sayed MA. Beating cancer in multiple ways using nanogold. Chem. Soc. Rev. 2011; 40(7):3391–3404. [PubMed: 21629885] * Review of Gold nanoparticle mediated therapy.
10. Bardhan R, Lal S, Joshi A, Halas NJ. Theranostic nanoshells: From probe design to imaging and treatment of cancer. Accounts Chem. Res. 2011; 44(10):936–946. * Review of gold nanoshell synthesis and imaging constrast engineering.
11. Chen W, Bardhan R, Bartels M, et al. A molecularly targeted theranostic probe for ovarian cancer. Mol. Cancer Ther. 2010; 9(4):1028–1038. [PubMed: 20371708]
12. Bardhan R, Chen W, Bartels M, et al. Tracking of multimodal therapeutic nanocomplexes targeting breast cancer in vivo. Nano Lett. 2010; 10(12):4920–4928. [PubMed: 21090693]
13. Bardhan R, Chen W, Perez-Torres C, et al. Nanoshells with targeted simultaneous enhancement of magnetic and optical imaging and photothermal therapeutic response. Adv. Func. Mater. 2009; 19(24):3901–3909. * First report of magneto-fluorescent gold nanoshells.
14. Argani P, Rosty C, Reiter RE, et al. Discovery of new markers of cancer through serial analysis of gene expression: Prostate stem cell antigen is overexpressed in pancreatic adenocarcinoma. Cancer Res. 2001; 61(11):4320–4324. [PubMed: 11389052]
15. Han H, Bearss DJ, Browne LW, Calaluce R, Nagle RB, Von Hoff DD. Identification of differentially expressed genes in pancreatic cancer cells using cDNA microarray. Cancer Res. 2002; 62(10):2890–2896. [PubMed: 12019169]
16. Iacobuzio-Donahue CA, Ashfaq R, Maitra A, et al. Highly expressed genes in pancreatic ductal adenocarcinomas: A comprehensive characterization and comparison of the transcription profiles obtained from three major technologies. Cancer Res. 2003; 63(24):8614–8622. [PubMed: 14695172]
17. Laurell H, Bouisson M, Berthelémy P, et al. Identification of biomarkers of human pancreatic adenocarcinomas by expression profiling and validation with gene expression analysis in endoscopic ultrasound-guided fine needle aspiration samples. World J. Gastroentero. 2006; 12(21):3344–3351.
18. Missiaglia E, Blaveri E, Terris B, et al. Analysis of gene expression in cancer cell lines identifies candidate markers for pancreatic tumorigenesis and metastasis. Int. J. Cancer. 2004; 112(1):100–112. [PubMed: 15305381]
19. Moniaux N, Chakraborty S, Yalniz M, et al. Early diagnosis of pancreatic cancer: Neutrophil gelatinase-associated lipocalin as a marker of pancreatic intraepithelial neoplasia. Brit. J. Cancer. 2008; 98(9):1540–1547. [PubMed: 18392050] * First report of clinical validation of NGAL as an early pancreatic cancer diagnosis marker.
20. Furutani M, Arii S, Mizumoto M, Kato M, Imamura M. Identification of a neutrophil gelatinase-associated lipocalin mRNA in human pancreatic cancers using a modified signal sequence trap method. Cancer Lett. 1998; 122(1–2):209–214. [PubMed: 9464512]
21. Tong Z, Kunnumakkara AB, Wang H, et al. Neutrophil gelatinase-associated lipocalin: A novel suppressor of invasion and angiogenesis in pancreatic cancer. Cancer Res. 2008; 68(15):6100–6108. [PubMed: 18676832]
22. Roy R, Louis G, Loughlin KR, et al. Tumor-specific urinary matrix metalloproteinase fingerprinting: Identification of high molecular weight urinary matrix metalloproteinase species. Clin. Cancer Res. 2008; 14(20):6610–6617. [PubMed: 18927302]
23. Iannetti A, Pacifico F, Acquaviva R, et al. The neutrophil gelatinase-associated lipocalin (NGAL), a NF-κB-regulated gene, is a survival factor for thyroid neoplastic cells. Proc. Natl. Acad. Sci. USA. 2008; 105(37):14058–14063. [PubMed: 18768801]
24. Lim R, Ahmed N, Borregaard N, et al. Neutrophil gelatinase-associated lipocalin (NGAL) an early-screening biomarker for ovarian cancer: NGAL is associated with epidermal growth factor-induced epithelio-mesenchymal transition. Int. J. Cancer. 2007; 120(11):2426–2434. [PubMed: 17294443]

25. Hu L, Hittelman W, Lu T, et al. NGAL decreases E-cadherin-mediated cellcell adhesion and increases cell motility and invasion through Rac1 in colon carcinoma cells. Lab. Invest. 2009; 89(5):531–548. [PubMed: 19308044]
26. Yang J, Bielenberg DR, Rodig SJ, et al. Lipocalin 2 promotes breast cancer progression. Proc. Natl. Acad. Sci. USA. 2009; 106(10):3913–3918. [PubMed: 19237579]
27. Leng X, Ding T, Lin H, et al. Inhibition of lipocalin 2 impairs breast tumorigenesis and metastasis. Cancer Res. 2009; 69(22):8579–8584. [PubMed: 19887608]
28. Hwang K, Houston JP, Rasmussen JC, et al. Improved excitation light rejection enhances small-animal fluorescent optical imaging. Mol. Imaging. 2005; 4(3):194–204. [PubMed: 16194451]
29. Gad SC, Sharp KL, Montgomery C, Payne JD, Goodrich GP. Evaluation of the toxicity of intravenous delivery of auroshell particles (gold-silica nanoshells). Int. J. Toxicol. 2012; 31(6): 584–594. [PubMed: 23212452]
30. Terentyuk GS, Maslyakova GN, Suleymanova LV, et al. Circulation and distribution of gold nanoparticles and induced alterations of tissue morphology at intravenous particle delivery. J. Biophotonics. 2009; 2(5):292–302. [PubMed: 19434616]
31. James WD, Hirsch LR, West JL, O'Neal PD, Payne JD. Application of INAA to the build-up and clearance of gold nanoshells in clinical studies in mice. J. Radioanal. Nucl. Chem. 2007; 271(2): 455–459.
32. Sengelov H, Boulay F, Kjeldsen L, Borregaard N. Subcellular localization and translocation of the receptor for N-formylmethionyl-leucyl-phenylalanine in human neutrophils. Biochem. J. 1994; 299(2):473–479. [PubMed: 8172608]
33. Nielsen BS, Borregaard N, Bundgaard JR, Timshel S, Sehested M, Kjeldsen L. Induction of NGAL synthesis in epithelial cells of human colorectal neoplasia and inflammatory bowel diseases. Gut. 1996; 38(3):414–420. [PubMed: 8675096]
34. Bratt T, Ohlson S, Borregaard N. Interactions between neutrophil gelatinase-associated lipocalin and natural lipophilic ligands. BBA-Gen. Subjects. 1999; 1472(1–2):262–269.
35. Schmidt-Ott KM, Mori K, Jau YL, et al. Dual action of neutrophil gelatinase-associated lipocalin. J. Am. Soc. Nephrol. 2007; 18(2):407–413. [PubMed: 17229907]
36. Galis ZS, Sukhova GK, Lark MW, Libby P. Increased expression of matrix metalloproteinases and matrix degrading activity in vulnerable regions of human atherosclerotic plaques. J. Clin. Invest. 1994; 94(6):2493–2503. [PubMed: 7989608]
37. Gough PJ, Gomez IG, Wille PT, Raines EW. Macrophage expression of active MMP-9 induces acute plaque disruption in apoE-deficient mice. J. Clin. Invest. 2006; 116(1):59–69. [PubMed: 16374516]
38. Loftus IM, Naylor AR, Goodall S, et al. Increased matrix metalloproteinase-9 activity in unstable carotid plaques: A potential role in acute plaque disruption. Stroke. 2000; 31(1):40–47. [PubMed: 10625713]
39. Te Boekhorst BC, Bovens SM, Hellings WE, et al. Molecular MRI of murine atherosclerotic plaque targeting NGAL: A protein associated with unstable human plaque characteristics. Cardiovascular Res. 2011; 89(3):680–688.
40. Ghaneh P, Costello E, Neoptolemos JP. Biology and management of pancreatic cancer. Postgrad. Med. J. 2008; 84(995):478–497. [PubMed: 18940950]
41. Schwartzberg AM, Olson TY, Talley CE, Zhang JZ. Synthesis, characterization, and tunable optical properties of hollow gold nanospheres. J. Phys. Chem. B. 2006; 110(40):19935–19944. [PubMed: 17020380]
42. Bardhan R, Mukherjee S, Mirin NA, Levit SD, Nordlander P, Halas NJ. Nanosphere-in-a-nanoshell: A simple nanomatryushka. J. Phys. Chem. C. 2010; 114(16):7378–7383.

Executive summary

Introduction

- Neutrophil gelatinase associated lipocalin (NGAL) is a promising marker for early diagnosis of pancreatic intraepithelial neaoplasia.
- Theranostic gold nanoshells (TGNS) allow MRI/fluorescence optical imaging and photothermal therapy.
- Antibody conjugated TGNS for targeting NGAL overexpressing Pancreatic Cancer was investigated.

TGNS characterization

- TGNS are composed of plasmonic gold nanoshells with a silica epi-layer doped with iron oxide/indocyanine green that enable photothermal therapy with enhanced MRI/NIR-fluorescence imaging of cancer with FDA cleared components.

AntiNGAL-conjugated TGNS bind pancreatic cancer cells *in vitro* to facilitate photothermal therapy

- TGNS nanocomplexes are nontoxic to cancer cells in the absence of laser-mediated activation of photothermal heating.
- AntiNGAL-conjugated TGNS specifically bind to AsPC-1 human pancreatic cancer cells and thus mediate targeted photothermal therapy and MRI/NIR-fluorescence imaging *in vitro*.

AntiNGAL-conjugated TGNS enhances accumulation in tumor possibly by interacting with NGAL

- AntiNGAL-conjugated TGNS enable specific targeting of pancreatic cancer xenografts (AsPC-1 cell line) in mice following systemic delivery.
- Circulation of molecularly targeted TGNS has been tracked *in vivo* using MRI and NIR-fluorescence imaging.
- AntiNGAL-conjugated TGNS enable imaging of pancreatic tumors with higher contrast with both NIR and MR imaging, and result in higher tumor deposition of gold than the non-conjugated TGNS.

Conclusion

- TGNS enabled molecularly targeted imaging and photothermal therapy of pancreatic cancer cells with expression of early disease marker NGAL.
- TGNS were successful for dual modality in vivo NIR-MR imaging of NGAL overexpressing Pancreatic Cancer in a subcutaneous tumor model.

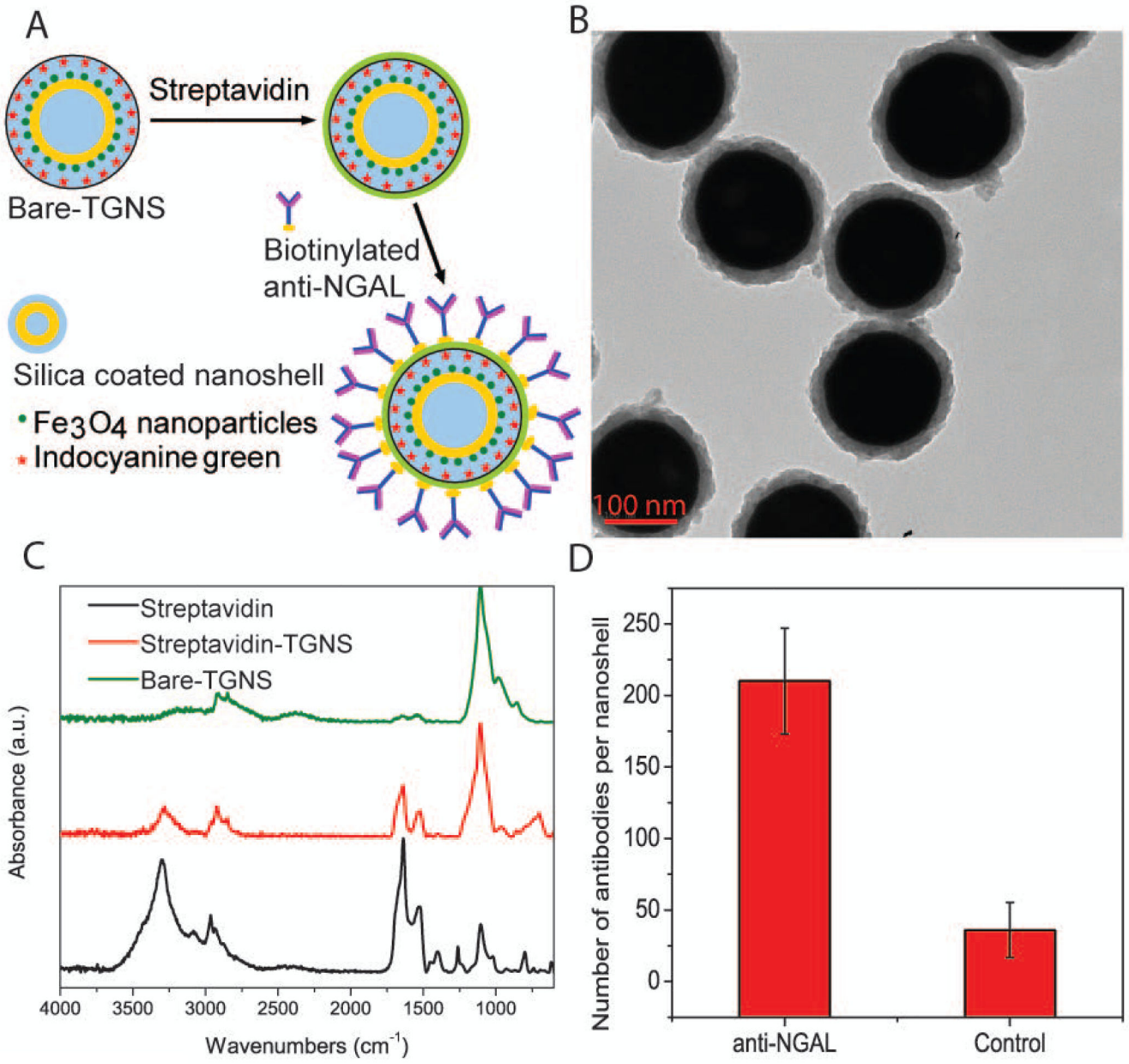

Figure 1.

Characterization of theranostic gold nanoshells (TGNS). A) Schematic representation of antibody (anti-NGAL) conjugation to theranostic gold nanoshell(TGNS). B) TEM image of the TGNS. The nanocomplex diameter is ~180 nm. Scale bar is 100 nm. C) FTIR spectrum of streptavidin-conjugated TGNS. The FTIR spectra of streptavidin and bare-TGNS are shown for comparison. D) Quantification of the number of antibodies on anti-NGAL-conjugated TGNS and control (bare-TGNS).

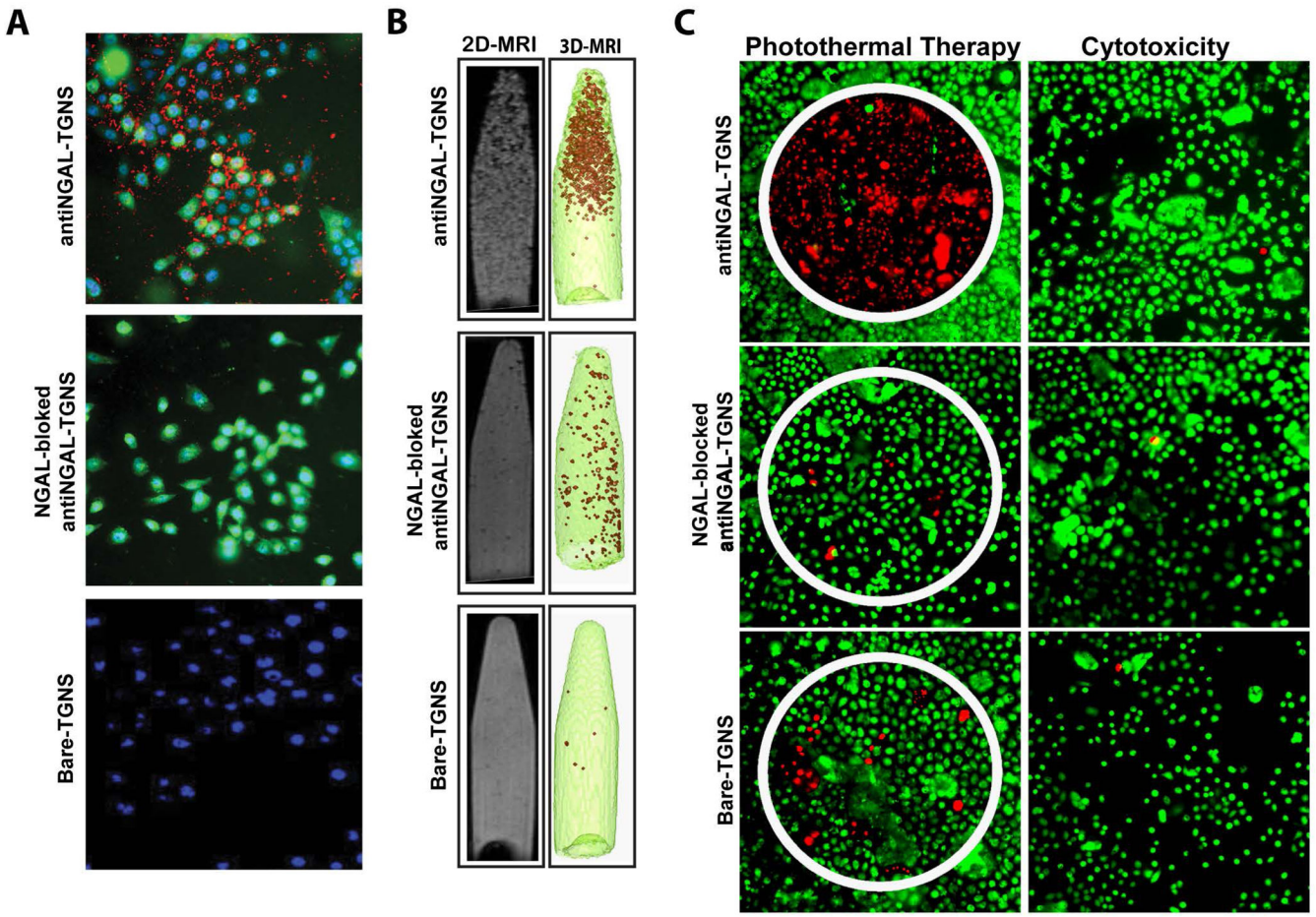

Figure 2.

(A) Fluorescence Imaging of NGAL-expressing AsPC-1 cells showing nuclei stained with DAPI (blue), immunolocalization of antiNGAL stained with a secondary antibody-Alexa-fluor 488 (green) and NIR fluorescence of ICG doped inside the silica layer of the antiNGAL-TGNS (red). Cells were incubated with antiNGAL-TGNS, NGAL was blocked with antiNGAL before adding antiNGAL-TGNS, cells were incubated with unconjugated-TGNS respectively. Specific binding was observed on the AsPC-1 cell surface for the antiNGAL-TGNS. (B) 2-D MR images of AsPC-1 cells suspended in 0.5% agarose. 3-D MRI maximum intensity projections of thresholded T2 maps of the images corresponding to 2-D MRI. 3-D MRI give a visual representation of cells labeled with the magnetic TGNS. (C) Photothermal ablation and live/dead stain of AsPC-1 cells. Cells were treated with NIR laser at 808nm for 10 min. Absence of cytotoxicity in AsPC-1 cells. Live cells are stained green with calcein and dead cells are stained red with propidium iodide. Original magnification: ×100 and scale bar is 250 μm for all panels.

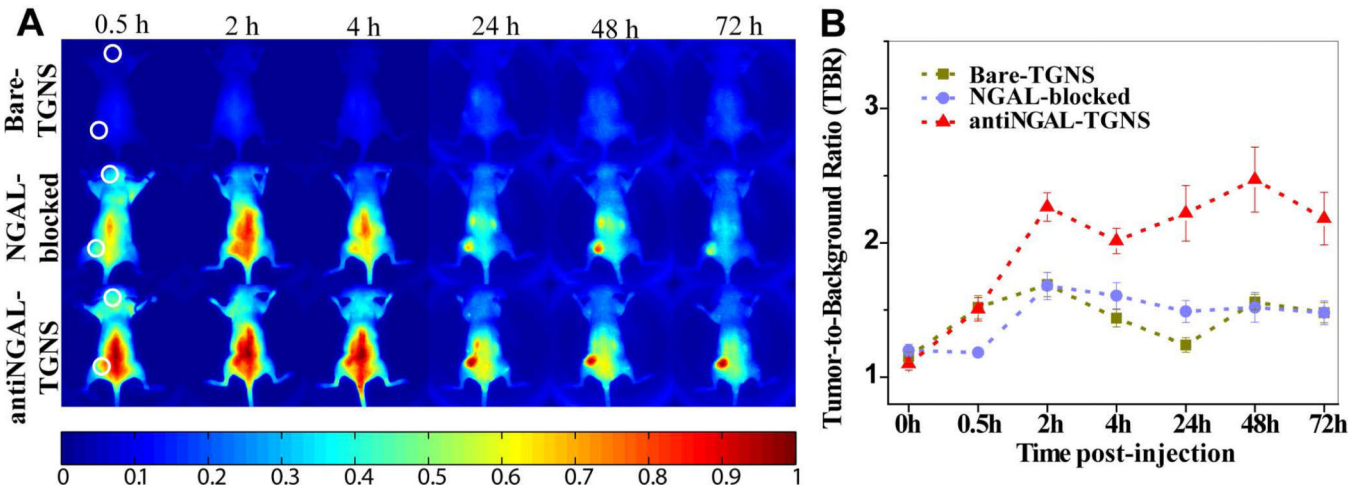

Figure 3.

(A) Delivery of nanocomplex *in vivo* and imaging via NIR-FOI in mice with overexpressing NGAL xenografts. NIR-FOI images of mice on top row were NGAL-blocked with prior antibody injection and treated with antiNGAL-TGNS (n=6), and bottom row were treated with antiNGAL-TGNS (n=7) at 0.5, 2, 4, 24, 48, and 72 h post-injection, respectively. (B) Tumor to background ratio (TBR) for each group of mice across the imaging time points. The statistical results show the TBR signal increases significantly at 24h compared to the two control groups.

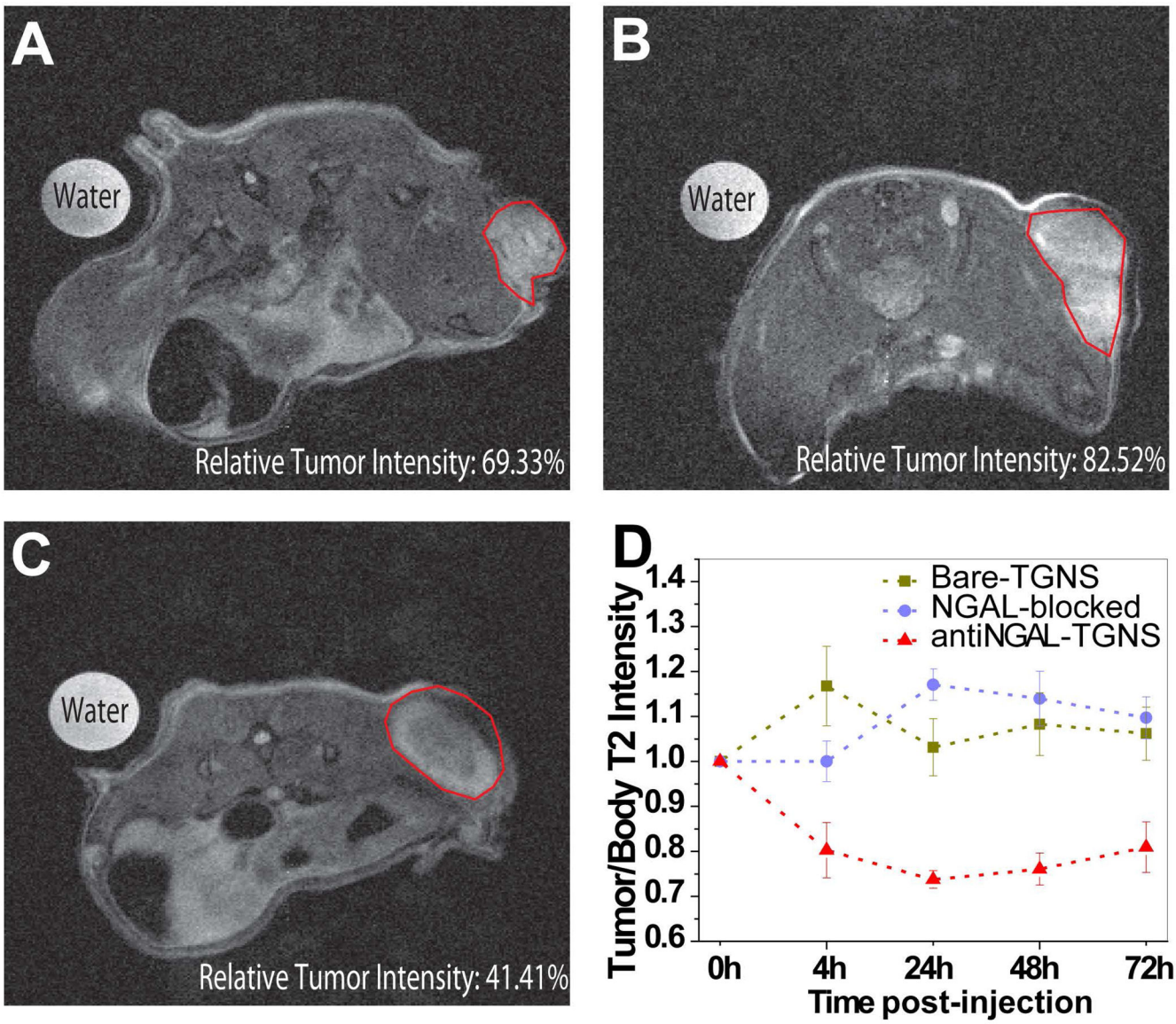

Figure 4.

(A) NGAL blocked prior to antiNGAL-TGNS injection (n=6). (B) antiNGAL-TGNS injection (n=7). (C) TBR of intensities across time points. MRI of mice cross-section and MR signal intensity analysis on tumors at 24 h post-injection. The statistical results showing the relative tumor intensity in antiNGAL-TGNS group (41.41%) is lower compared to NGAL-blocked (82.52%) group.

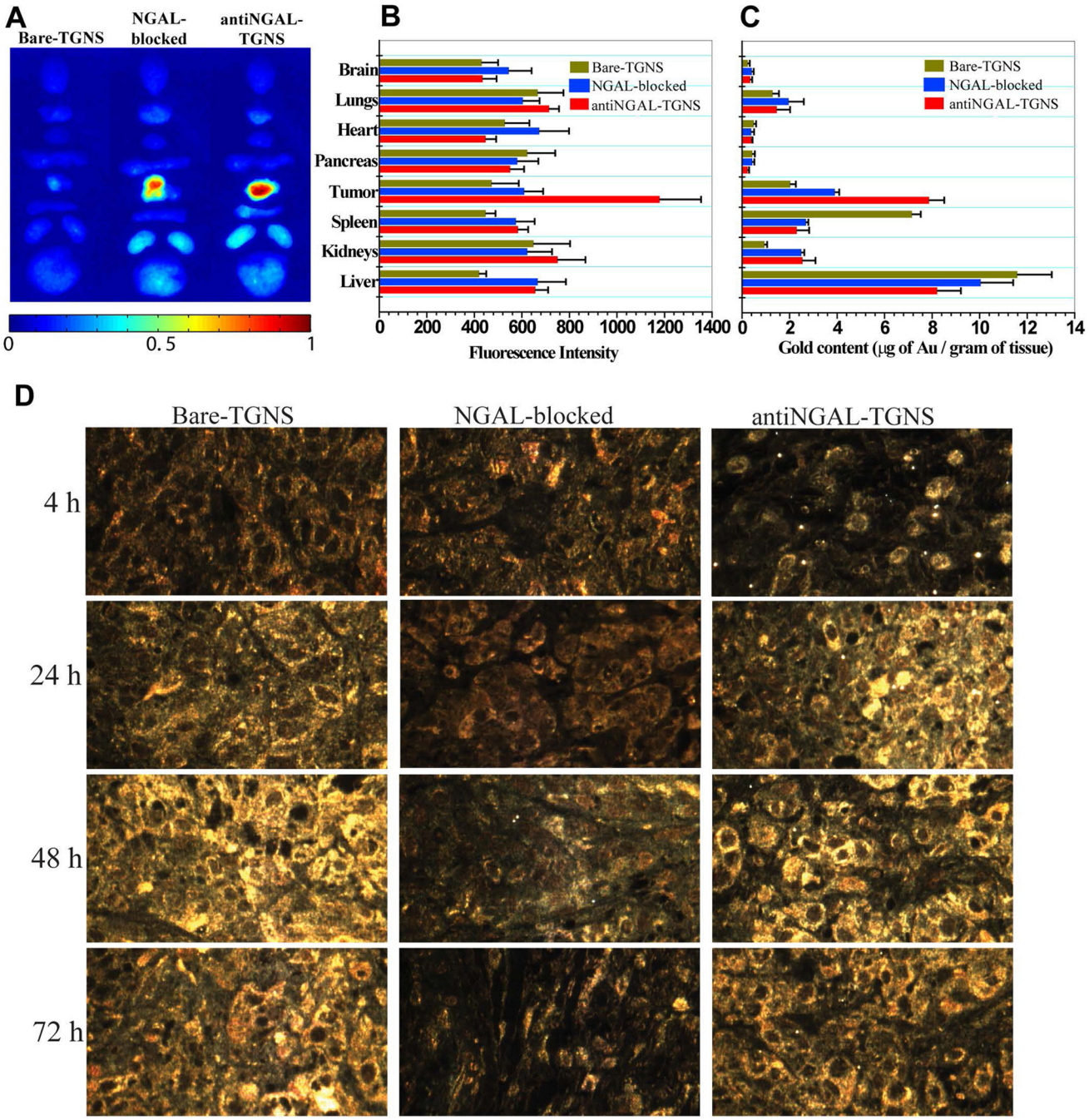

Figure 5.

Nanocomplex biodistribution in organs and xenografts of euthanized mice at 72 h post-injection. (A) NIR-FOI of representative mice organs. The fluorescence intensity is normalized with respect to the intensity in the tumor labeled as antiNGAL-TGNS. (B) Fluorescent intensity in each organ. (C) Gold content in each organ measured by ICP-MS. The results in various mice organs showing significant gold content in tumors. (D) Dark-field microscopy images of tumor tissue. Gold nanoshells strongly scatter light and thus generally are observed as bright spots in dark-field.

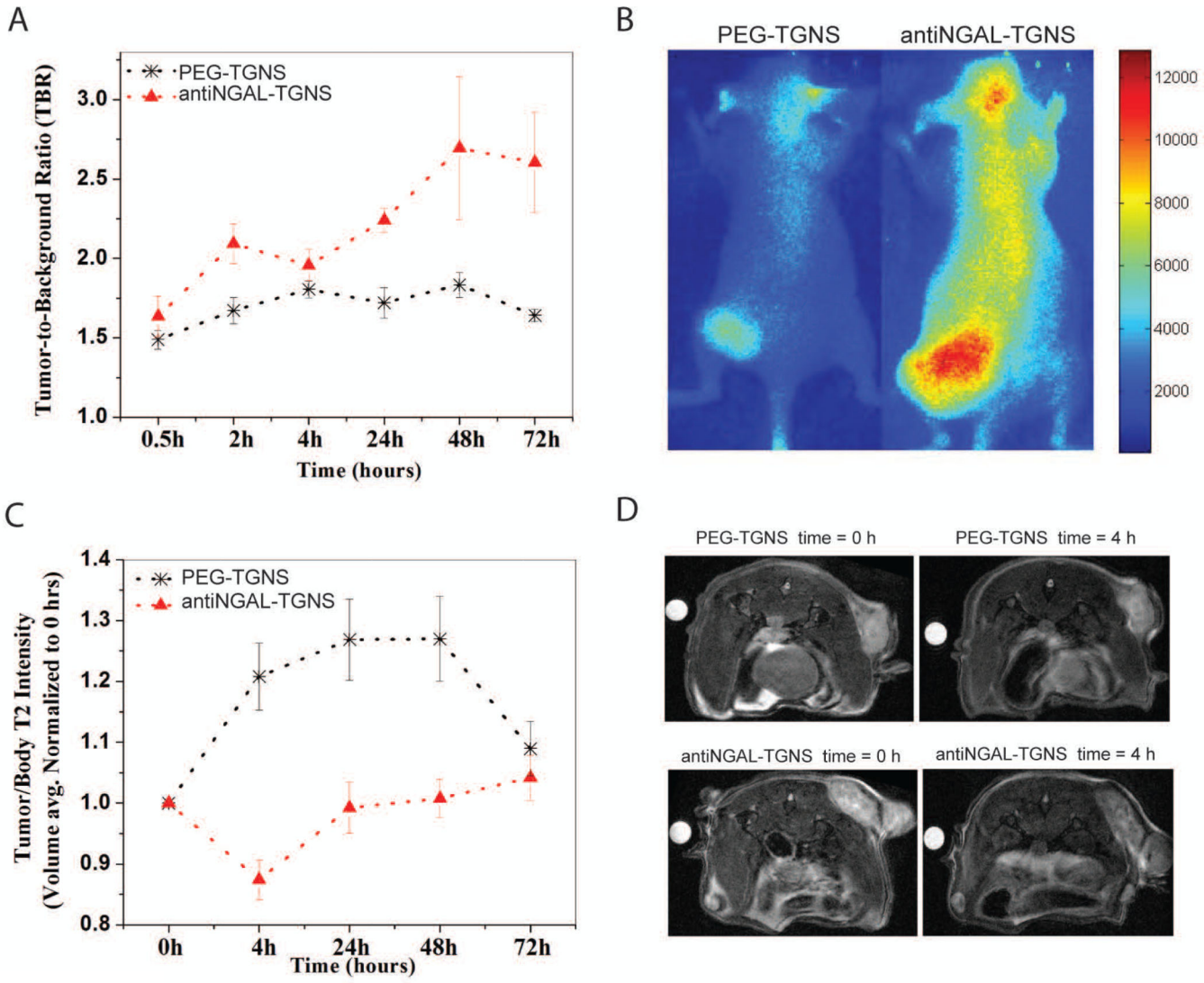

Figure 6.

Analysis of the NIR-fluorescence and T2 MRI contrast induced by accumulation of the theranostic gold nanoshells (TGNS) in pancreatic cancer tumors (AsPC1 cell line). A) TBR of fluorescence intensity for each group of mice across the imaging time points. B) Fluorescence Optical Imaging of mice at 24 h post-injection with PEGylated TGNS (PEG-TGNS, n=6) and anti-NGAL conjugated TGNS (antiNGAL-TGNS, n=6). C)Tumor to body ratio of T2 MRI intensities across time points. D) T2 MRI of mice before injection (0 h) and 4 h post-injection of PEG-TGNS and anti-NGAL-TGNS.